A new method for ultrasonic fatigue testing of equibiaxial and pure shear cruciform specimens

Pedro R. da Costa[1], Luís Reis[1,2], Diogo Montalvão[3], Manuel Freitas[2,4]

[1]Instituto Superior Técnico, Universidade de Lisboa, Av. Rovisco Pais, 1049-001 Lisbon, Portugal

[2]IDMEC, Instituto Superior Técnico, Av. Rovisco Pais, 1049-001 Lisbon, Portugal

[3]Department of Design and Engineering, Faculty of Science and Technology, Bournemouth University, Poole House, Talbot Campus, Fern Barrow, Poole BH12 5BB, United Kingdom

[4]Atlântica, Instituto Universitário, Fabrica da Pólvora, Barcarena, 2730-036 Barcarena, Portugal

Abstract

Mechanical and material testing and analysis are of indisputable importance. As the variety of materials and/or the complexity of products grows, so does the need for new material characterisation methods. In this study, experimental results from a new method for ultrasonic fatigue testing of equibiaxial and pure shear cruciform specimens is presented and validated. The method uses specially designed cruciform specimens' geometries for ultrasonic fatigue testing machines. Three different cruciform geometries were tested. The responses from the specimens were first studied by an adapted modal calculation method FDD. The new method allows determining fatigue strength of cruciform specimens in the VHCF regime with very satisfactory results.

Keywords

Ultrasonic fatigue; Cruciform specimens; Biaxial fatigue; VHCF; Fatigue in-plane

1. Introduction

The continuous study of materials under fatigue conditions and the development of new testing machines and methods for its characterisation proves its importance, not only in the scientific world but also for its industrial application. With the development of new materials and alloys, industry demands predictability of material properties that is reliable and obtained in a timely manner. Through its detailed characterisation, more complex designs with reduced weight and higher life spans can be achieved with increased reliability, confidence, and safety.

Conventional and standard fatigue testing methods apply force/strain/displacement cyclic loads and induce damage through electromechanical or servo-hydraulic machines. Low to high cycle fatigue regimes can be achieved by changing the load and stress state. Fatigue tests have been predominantly focused on inducing uniaxial loads. However, since most components and machines are subjected to multiaxial cyclic loads, many researchers have dedicated their studies to multiaxial technological developments and their fatigue properties [1].

As multiaxial fatigue inducing technics have increased in reliability and versatility towards the material and shape under analysis, so did the cyclic testing frequency. It was once considered that beyond 10^7 cycles (the fatigue limit) no failure would occur, i.e., materials would have infinite life. Takeshi et al. [2] observed for the first time continuous fatigue failure beyond 10^7 cycles in carburised steel. Bathias [3] and his research team have reinforced the non-existing fatigue failure limit at 10^6 to 10^7 cycles. Thereafter, failure arising beyond the believed fatigue limit was established to be within the Very High Cycle Fatigue (VHCF) regime, between 10^7 to 10^9 cycles [3–5].

Conventional fatigue testing machines have operational frequencies that typically vary between 10 Hz and 150 Hz. This means that it is not feasible to use them to test materials up to the VHCF regime. With the aim to induce damage at higher fatigue regimes, Ultrasonic Fatigue Testing (UFT) was developed using resonance principles to reach high enough strains in very high frequency. Mason developed the ultrasonic fatigue machine setup with a working frequency of 20 kHz. His setup and frequency were generally accepted as the norm and are followed by almost all recent researches using UFT machines [4]. Since Mason, a high range of materials have been tested in all basic uniaxial testing methods as tension-compression [6], bending [7], and torsion [8; 9]. In a comprehensive study, Costa et al. [10] discuss the latest developments in multiaxial fatigue specimens and testing methods from conventional to ultrasonic fatigue, with an emphasis on the biaxial fatigue method used in this study.

In the present work, cruciform fatigue specimens are tested in the VHCF regime. The testing methodology has been devised to work in UFT machines, inducing an axial-axial biaxial stress state at a 20 kHz frequency. The cruciform axial-axial testing methods are of increasing importance for material biaxial response characterisation. Cláudio et al. and Shanyavskii [11; 12] have shown its importance in aluminium alloys, while Smits et al. and other researchers [13; 14] have demonstrated its importance for composites characterisation through extensive testing in composite materials.

1.1 Ultrasonic cruciform fatigue testing

The development of UFT machines began with primary uniaxial tension-compression machines [15]. The current focus is on the development of multiaxial UFT methods. C. Brugger et al. [16] proposed a multiaxial bending method through inducing bending resonance to a disk-shaped specimen. Costa et al. [17] developed three throat specimens able to reach axial-torsion stress states at ultrasonic frequencies. In this study, a multiaxial method is presented and analysed through the use of cruciform specimens first designed by D. Montalvão and A. Wren [18]. All tested cruciform specimens were machined from 6082-T651 aluminium. This is a medium strength Al. alloy with a fibrous core microstructure that is heat treatable with high corrosion resistance rate. It is used in many highly stressed engineering applications, including trusses, cranes, bridges, and transportation. It also has excellent extrudability which helps in the manufacturing and machining of the specimens or components.

The developed cruciform specimens induce an axial-axial stress state with an axial stress ratio B = 1 (equibiaxial) for in-phase Tension-Tension cruciform specimens (T-T), and B = -1 (pure shear) for out-of-phase Compression-Tension cruciform specimens (C-T). New specimens have also been proposed capable of achieving non-unitary biaxial stress ratios, both in-phase and out-of-phase [19], but they were not tested in this study.

Three different cruciform specimens were tested in the present work: the original and **F**irst in-phase **T-T** specimen (**F*x* T-T**) [20]; a **N**ew in-phase **T-T** specimen (**N*x* T-T**), where the found problems in the original T-T were considered and improved in the FEA designing process; and the out-of-phase **C-T** specimens (**C-T *x***). Table 1 shows the cruciform specimens under discussion and their respective designations.

Table 1. Cruciform specimen's designations.

Original in-phase F*x* T-T	New designed in-phase N*x* T-T	Out-of-phase C-T *x*
F1 T-T	N1 T-T	C-T 1
F2 T-T	N2 T-T	C-T 2
F3 T-T		C-T 3

The cruciform geometries were designed following the Baptista et al. [21] optimised geometry. The reached dimensional relations were made for low size, low thickness specimens, ensuring the maximum stress on its midpoint. Finite Element (FE) modal analysis was used to determine the ultrasonic cruciform dimensions in such a way that the desired resonant mode shape reach 20 kHz. All tested geometries were already induced in resonance with a respective extensively analysed response outcome through FE [20]. The New N T-T specimens were made with considerably higher dimensions, which has improved dimensional quality from the machining process. The overall increased dimensions made easier the machining process of the midpoint reduced section area, resulting in higher quality and corresponding low variability. Figure 1 presents Baptista et al. [21] geometry and all three tested cruciform geometries.

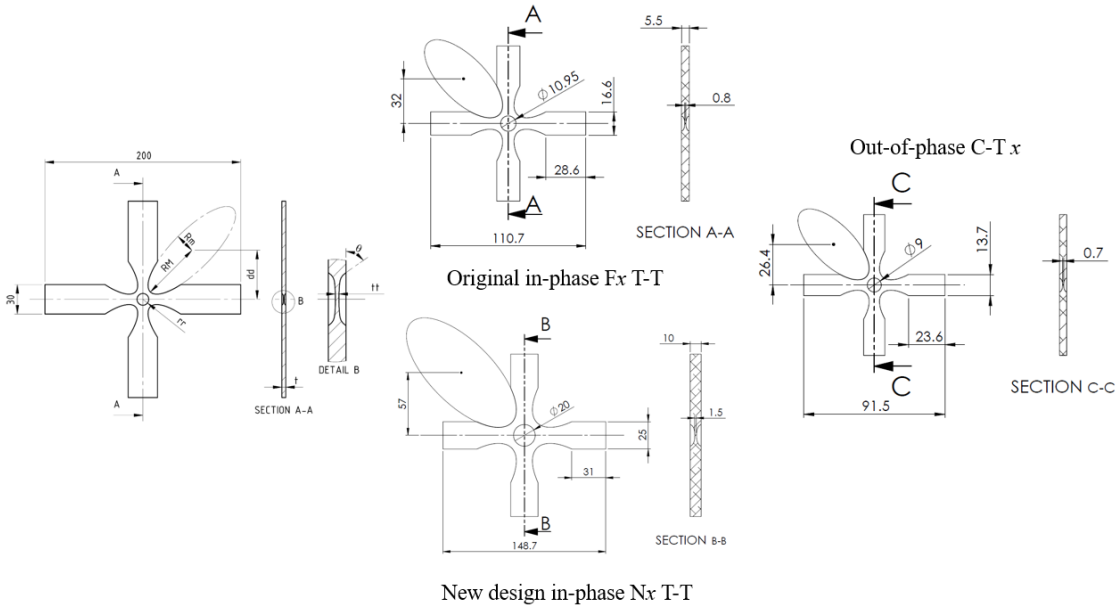

Fig. 1. Baptista et al. [21] geometry; All three tested cruciform geometries with key dimensions [mm].

All specimens were lightly polished in the midpoint reduced section area. Due to the smaller F*x* T-T and C-T *x* overall midpoint section size, the polishing process almost reach a full mirror-like surface. For the New N x T-T specimens, the increased size allowed for a mirror-like polishing process in the midpoint section. Other elliptical geometries were later perceived as essential to be treated before testing, as it will be later analysed and explained.

While C-T specimens showed a promising behaviour, the first F*x* T-T specimens showed undesired displacements linked to a "parasite" resonant mode in the vicinity of the UFT machine's operating frequency. This parasite mode shape was found to adversely affect the stresses being generated at the centre of the specimens. Therefore, a novel T-T specimen was redesigned taking into consideration the parasite mode presence, the N*x* T-T specimen. Two resonant modes were under analysis for all tested specimens characterised as the Mode of Interest (MI) and the Parasite Mode (PM). Figure 2 shows the deformation associated with both mentioned modes.

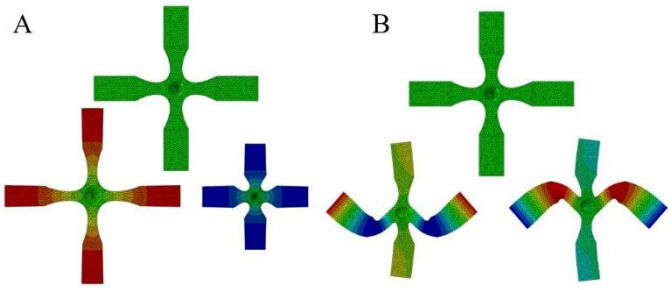

Fig. 2. Cruciform in-phase T-T resonant mode shapes: (A) Mode of interest MI; (B) Parasite mode PM [20].

To achieve the improved Nx T-T specimen, FEA analysis were iteratively conducted with changing dimensions, maintaining the followed Batista et al. dimensional relations. The combination with the highest frequency difference between MI and MP was chosen.

The resonance behaviour of the specimens, induced strains and initial fatigue tests were carried out. Experimental data was used to validate the specimens' MI and PM behaviour, as observed in the FE models. The modal analysis was conducted by adapting an existent output-only modal analysis method used in structures under unknown loads. The Frequency Domain Decomposition (FDD) method was firstly developed for buildings and bridges where the force input, like the one produced from cars or wind, is unmeasurable [22]. One limitation of the UFT method currently available and used in this

research is the unknown cyclic excitation force. Partly due to the s conducted resonance excitation method and overall setup size, no known method to date can measured the excitation force applied to the specimen.

Strain measurements at the specimen's centre were made through rosette strain gauges. Strain gauges were only applied to those specimens showing the closest behaviour to the one predicted by FE analysis. Several samples of the three cruciform geometries under study were put under UFT until failure.

2. Modal analysis

As aforementioned, all different cruciform geometries were subjected to a modal FDD analysis. The FDD method requires only output measurements. A stepwise frequency scan set excitation was conducted within the piezoelectric transducer frequency range (20±0.5 kHz). The output response was measured using a dual-channel LASER Doppler vibrometer. The response coordinates are at the cruciform ends, as shown in Figure 3, i.e., where the two intended modes' highest displacement are located. Three different measurement points were determined based on the FEA results of the cruciform specimens with the horn and booster set assembly. Due to the inability to measure three displacement locations simultaneously, two different runs were conducted, setup A and B, see Figure 3.

Concerning the setups for measuring, setup A focuses on two measurement points where both modes under analysis have high displacements: Laser 1 (L1) measures the vertical displacement on the vertical arm (following the horn axis) for the MI; laser 2 (L2) measures the vertical displacement of the horizontal arm associated with the PM; Laser setup B associates the displacement axial-axial ratio between vertical and horizontal arms having Laser 1 measuring vertical displacement on the vertical arm and Laser 3 (L3) measuring the horizontal displacement of the horizontal arm.

Since L1 location and displacement direction is coincident between the two modes, it was established as the reference measuring point between setups A and B. Figure 3 shows an ultrasonic set representation and the experimental laser setups A and B described previously.

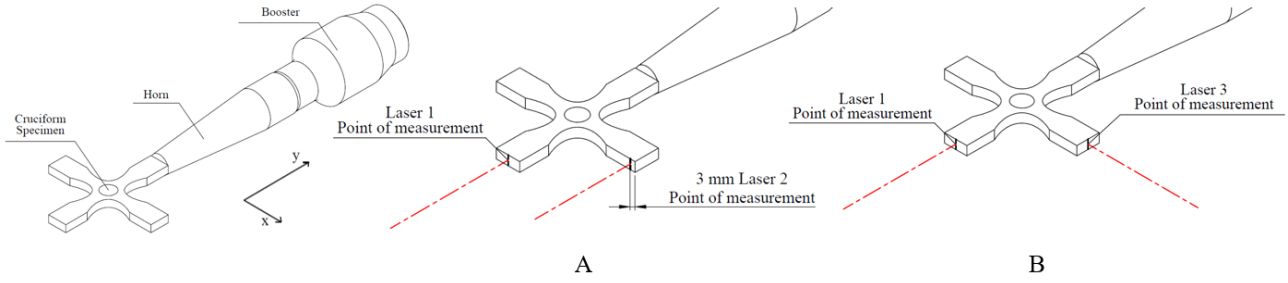

Fig. 3. Laser setups for both runs: A and B.

From the output signal's observation, the MI or/and the PM are observable in all tested specimens. The resonant modes are observable where the displacement is significantly higher throughout the frequency scan. Figure 4 shows setup A and B stepwise frequency scan output for the F1 T-T, and N1 T-T specimens and identifies both the MI and PM. In respect to the MI, the PM has a lower frequency for F1 T-T specimen, and higher frequency for N1 T-T specimen. From Figure 4 F1 and N1 T-T laser results present the MI and PM within the transducer frequency range. The MI is associated with higher overall amplitude for L1 and L3, while the PM presents higher L2.

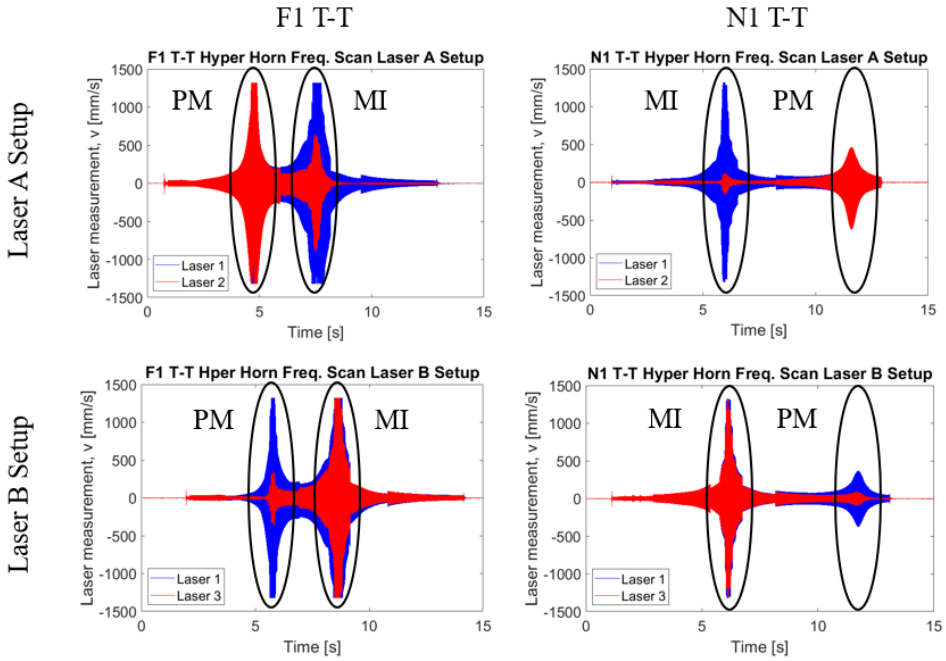

Fig. 4. Frequency scan laser setup A and B results for F1 T-T and N1 T-T specimens.

A clear PM amplitude difference of both L1 and L3 is perceived between the original F1 and new N1 T-T specimen. Following the FDD method, the power spectral density (PSD) is first calculated from the measured output. The resonance modes frequency is determined from the observable PSD peaks. The calculated PSD magnitude to frequency results shown in Figure 4 frequency scans is presented now in Figure 5.

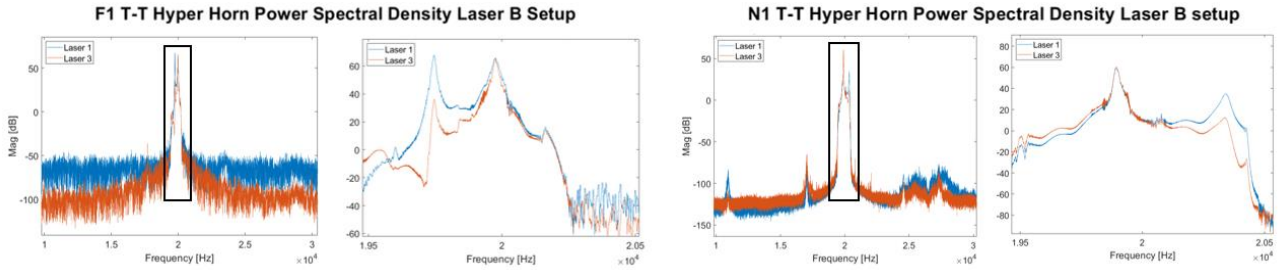

Fig. 5. PSD Mag/frequency F1 T-T and N1 T-T result in laser B setup with a respective enlarged view in the transducer frequency range.

Singular value decomposition (SVD) is afterwards calculated from the presented Figure 5 PSD results. SVD allows the modal shape determination for the measured coordinates in each taken PSD peak. FDD has shown a higher and more consistent MI to PM difference in the New T-T specimens than the original T-T specimens. While in the F1 T-T the frequency difference between modes is ~-1% (180 Hz), the new specimens have a higher ~+2% (330 Hz) difference. The small improvement proved quite significant in terms of the PM impact on the MI deformed shape. The closer frequency proximity of the PM translates into displacement amplitude amplification as measured from L2 in the MI and higher variability between axial-axial ratio displacements (L1/L3). Comparing the N1 T-T and the F1 T-T, the vertical displacement at the horizontal arms (L2) proved to be less than half to the vertical arms (L1) in MI. A clear improvement was achieved.

FDD calculation method proved capability to determine different resonant modes far from the frequency range of the transducer with good frequency compliance to the one determined by FE frequency analysis. The C-T specimens showed the PM outside the frequency transducer range with a ~+11% (2200 Hz) difference in respect to the MI, as expected by FE analysis. It was only possible to experimentally determine its frequency and mode shape by the FDD method.

For C-T and New T-T geometries, resonance frequencies and associated mode shapes (displacement ratios) are consistent for both MI and PM from one specimen to another. In contrast, the original T-T specimens presented a greater frequency

variability of both modes. One single first F3 T-T specimen showed a high ~-4% (700 Hz) MI to PM frequency difference. Its mode shape proved a similar behaviour to new T-T and C-T specimens. A rosette strain gauge was applied to this specimen.

The original T-T specimens proved variable frequency results having both MI and PM, only MI and only PM mode within the working range of the transducer. The frequency scan and FDD magnitude vs frequency result for the first F2 T-T specimen with just the PM is shown in Figure 6. MI is not perceived in the recorded output signal, but it is revealed by FDD methods. MI and PM are identified in the PSD respective peaks presented in figure 6.

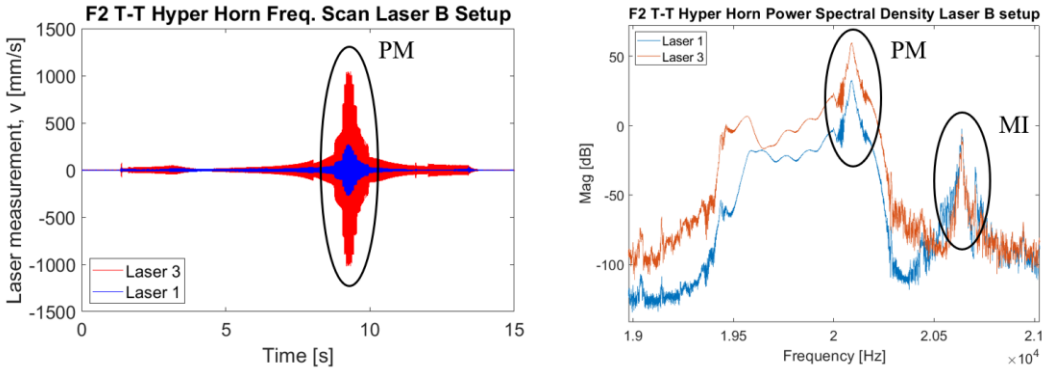

Fig. 6. Frequency scan and respective PSD calculation of the F2 T-T specimen with only PM within the piezoelectric frequency range.

Specimens with only PM within the transducer frequency range show the FDD method interest and the mode shape resulting negative impact on the specimen-horn connection. PM mode has deformation in the specimen-horn connection, which has led to unscrewing or even connection fracture. Therefore, all F T-T specimens were modified in the connection region to improve the horn connection enabling test under high enough power settings to reach fatigue failure. The improved connection presented no frequency and neither modal shape behaviour change.

Amplitude phase between each measured point was also determined by the FDD method. Both, the setup B and setup A signals phase were determined. Setup B proved the T-T in-phase and C-T out-of-phase. Setup A phase will influence the L3 amplitude. The manner to which it affects the L3 amplitude magnitude will be better comprehended in next section (section 3).

3. Strain and displacement measurements

Along with the conducted FDD analysis, power/displacement experiments in A and B laser setups were conducted. Afterwards, strain gauges were applied at the centre of several specimens. For each laser setup and strain measurements, five and ten power transducer settings were performed with a hyperbolic and Tapered horn setup, respectively. Differently from FDD frequency scans, the excitation occurs at a constant frequency. The excitation frequency is, for MI only or MI and PM specimens (within the transducer working frequency), the respective MI frequency. Contrarily, PM only specimens were excited in resonance in their respective PM frequency. For each power setting, the displacement amplitudes and the strain values were taken from the laser vibrometer and rosette strain gauges, respectively. Figure 7 shows the Laser B experimental setup power-displacement result for F1 T-T, N1 T-T, and a C-T 1 specimens. Figure 7 Laser B setup results were obtained with both tapered and hyperbolic horn sets.

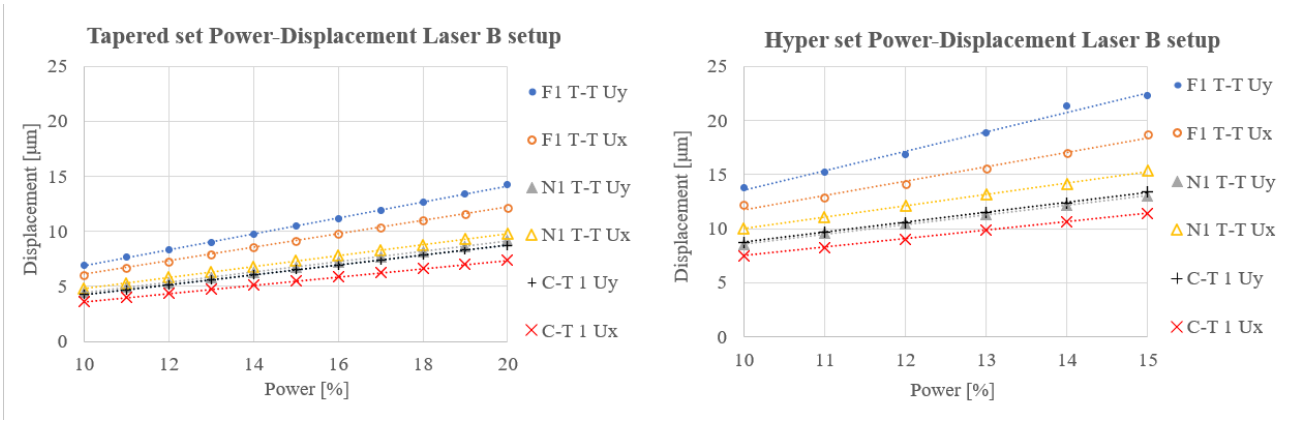

Fig. 7. Both tapered and hyperbolic horn Laser B setup displacement amplitude for different transducer power settings.

F1 T-T specimen shows a considerably higher displacement amplitude in both *x* and *y* directions. Such behaviour is due to the proximity of the PM. The increased displacement amplitude is parallel to the measured amplitude in F T-T specimens with only the PM within the transducer frequency range, as the F2 T-T showed in figure 6.

F1 T-T average difference between *x* and *y* displacement amplitude is also higher. It has a 14% and 20% average difference for the tapered and hyperbolic set, respectively, while the N1 T-T specimen has 7% and 14%, and the C-T 1 14% and 16% difference. Only the F3 T-T specimen with a high MI to PM frequency difference presented a similar behaviour to New T-T and C-T specimens. It showed an even lower *x y* amplitude difference of 3% for both hyper and tapered horn.

Between UFT specimens, especially under multiaxial loadings, minor dimensional variations led to variations in power/displacement relation. But the significant amplitude increase and higher difference present in the F1 T-T specimen is too high to be neglected without considering outside interference.

An amplitude difference between *x* and *y* is present in all specimens. The difference is expected, even with a considerably high MI to PM frequency difference (as C-T specimens have shown to have). As discussed in the Costa et al. [20], the induced 'flapping' motion of the specimen's horizontal arms is associated with its frequency difference to the working ultrasonic set. The frequency difference leads to a displacement node adjustment creating the 'flapping' motion. As the frequency difference increases the 'flapping' associated displacement amplitude will also increase tending towards the PM.

From Figure 7 close observation, the *x* displacement is lower than *y* in the F1 T-T and C-T 1 specimen, while the N1 T-T specimen has higher *x* displacement. The 'flapping' motion phase to L1 will result in a lower *x* to y amplitude when in-phase, as for F1 and C-T 1, and vice-versa in out-of-phase, as in N1.

Power-displacement measurements made with Laser A setup reinforce the PM interference determined by Laser B setup. F1 T-T specimen has considerably higher L2 amplitudes to those measured by all new N T-T and C-T specimens. Figure 8 presents power/displacement results in laser A setup for the same specimens compared in figure 7.

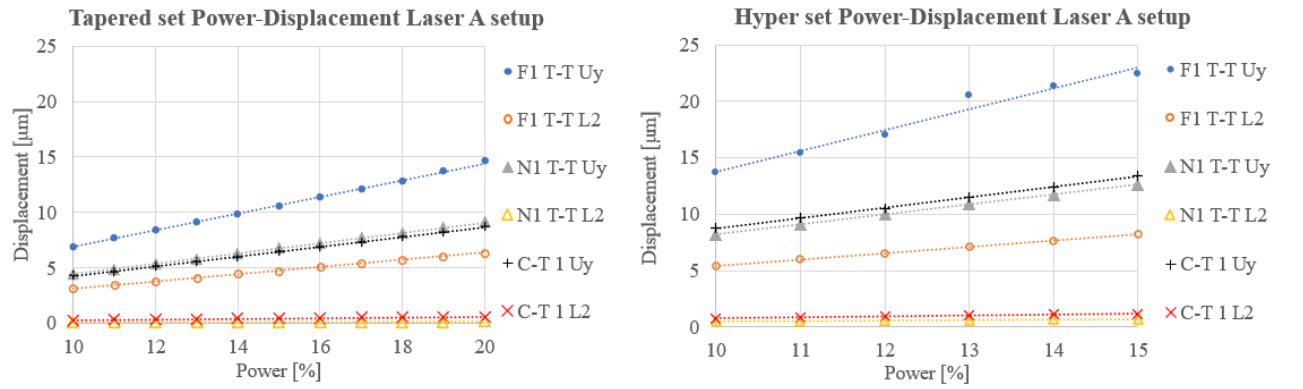

Fig. 8. Laser A setup displacement amplitude for several transducer power setting on both tapered and hyperbolic horn sets.

In summary, for the F1 T-T specimen, the detrimental influence of the PM is noticeable on (i) the interference with the MI shown on FDD results; (ii) the *x* and *y* higher displacement amplitudes and (iii) disproportion and (iv) the considerable L2 displacement amplitude. On the contrary, for the New T-T and C-T specimens, the negligible influence of the PM is demonstrated on the same four criteria.

From the laser power-displacement measurements and FDD modal results, rosette strain gauges were attached to the cruciform's midpoint. Strain gauges were only used in specimens proving a neglectable PM influence and closer behaviour to FE analysis. The strain gauges were aligned with the induced *x/y* stress tension-tension and tension-compression. The same transducer power settings were again applied, and the strain values recorded. Again, both horns sets were used. Strain results were subsequently transformed to stress values through Hook's law. Figure 9 shows stress results for the same N1 and C-T 1 tested in Figure 7, and for the only original working F3 T-T specimen.

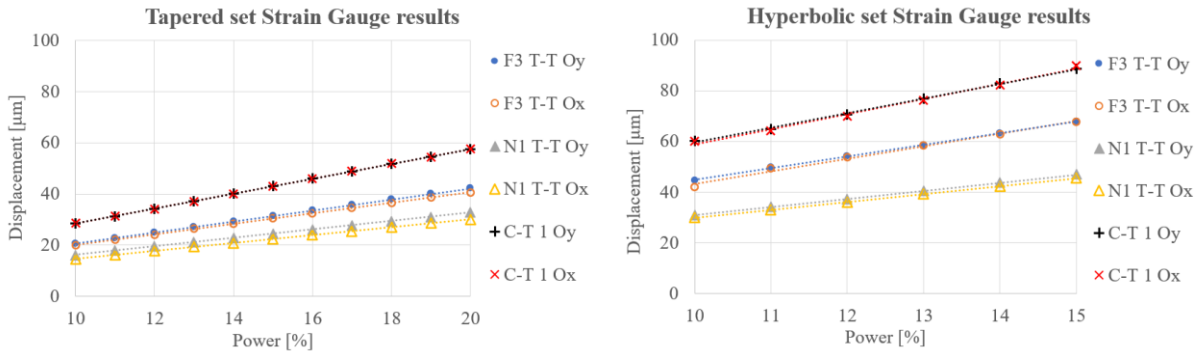

Fig. 9. Stress axial-axial (x-y) amplitude for several transducer power setting on both tapered and hyperbolic horns sets.

The *x* stress values are lower in all tested specimens. This is expected since the flapping motion of the cruciform specimen will mostly affect the horizontal arms deformation shape. Still, the average difference is acceptable, being: 3% and 0.5% in the First F3 T-T with the Tapered and Hyperbolic set, respectively; 8% and 4% for the N1 T-T; 1% and 0.5% for the C-T specimens.

The same frequency scan method used in the FDD method was also conducted while measuring strain. The results show the predicted neglectable PM influence in the final midpoint induced stress amplitude. Again, the neglectable influence of the PM in New T-T and C-T specimens was reinforced, and the final fatigue experiments began.

4. Fatigue testing

UFT were conducted on specimens having only either the PM or the MI within the frequency range. All fatigue experiments were conducted with considerably higher cyclic transducer power than the presented displacement and stress experimental results.

When testing at high stresses most ultrasonic specimens exhibit heat generation. The generated heat occurs due to the material damping and the high induced deformation or strain rate [23; 24]. The higher the strain amplitude more heat it generates. The overall generated heat can also vary between different tested materials/microstructures. When testing in ultrasonic machines, temperature control is required as well as a cooling method. This will ensure a coherent fatigue test with no temperature effect on the results. Since considerable heat is generated at the highest strain locations, a thermal camera was used to prove the correct functioning of the specimens. A higher heat generation at the centre is prove of higher stress combination on the centre and thus a correct cruciform fatigue testing region. For PM affected cruciform specimens, a non-desirable higher heat generation on the arms corners has proven higher stress combination outside the cruciform centre. Figure 10 shows thermal images of parasite only (PM) and working as intended (MI) specimens together with the highlighted region predicted by FE analysis.

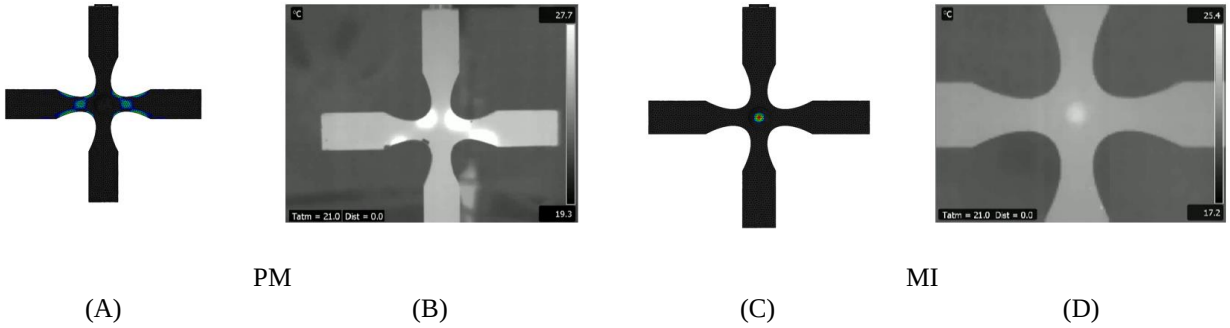

Fig. 10. FEA highest strain locations, (A) and (C), and resulting thermal imaging (B) and (D) for a PM and MI only specimens.

Observing Figure 10 (A), the PM specimen, the highest cycling strains occur at the arms' elliptical fillets and in the horizontal arms. Correlation between thermal imaging and FE results proves the predicted behaviour of the PM. UFT to F2 T-T (PM only within the transducer frequency range) induced fatigue cracks in all four fillets of the specimen. Figure 11 shows F2 T – T fatigue fracture, with induced fatigue cracks, fracture locations, and a detail fo crack initiation, see Figure 11 D. Some fatigue cracks propagated and reached the cruciform central circle. Halfway crack propagation, a change in behaviour was perceived, having a more linear and faster propagation behaviour.

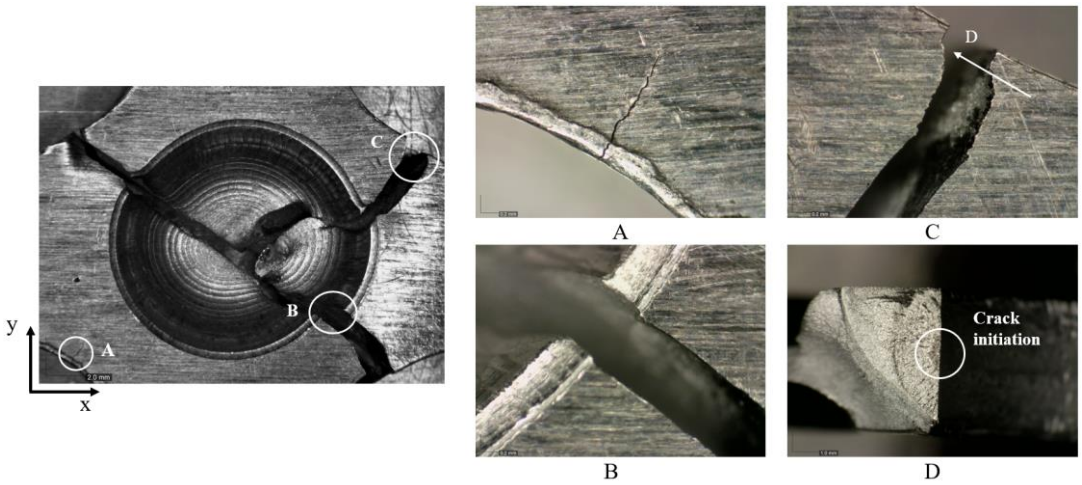

Fig. 11. PM only F2 T-T fatigue fracture: (A) induced fatigue crack; (B) and (C) crack initiation at the fillet; (D) detail of crack initiation.

Three C-T specimens, the only correctly working F3 T-T specimens, and two New T-T specimens were subjected to fatigue until failure. These are the cruciform specimens that prove a stress combination and modal shape of interest. All tested C-T, and F3 T-T specimens presented crack initiation at the central circle. Table 2 shows all fatigue lives concerning the applied stresses for all tested specimens. Stresses were determined in both; the *x* and *y* directions and the initial crack path direction is also shown. Fatigue life testing results tend to yield higher lives for lower stress combinations in all tested specimens.

Table 2. Fatigue testing life, stress, and angle results.

Specimen	σ_y [MPa]	σ_x [MPa]	θ(º)	Cycles
C-T 1	144.3	137.0	40.9	2.67E6
C-T 2	133.1	124.0	23.8	13.6E6
C-T 3	137.2	131.7	48.1	9.25E6
N1 T-T	112.47	107.07	-	12.1E6
N2 T-T	128.23	125.51	-	6.00E6
F3 T-T	176.48	174.96	51.2	0.76E6

Tested C-T specimens with 40º-50º degree crack initiation angle at the specimen's centre showed bifurcation on both ends (see Figure 12A and Figure 12B), while 23.8º degree crack initiation presented single crack growth, Figure 12C. The fracture result is consistent with previous studies on aluminium cruciform specimens. Through FE analysis, D. Infante-Garcia et al. [25] have determined the bifurcation effect when a 45º crack initiates in out-of-phase loadings. Considering the applied unitary biaxiality ratio, E. Lee and R. Tayler [26] showed that the initial crack path occurs at 45º. Wolf et al. [27] observed similar crack behaviour in aluminium cruciform specimens with 45º degree initial path leading to a similar bifurcation.

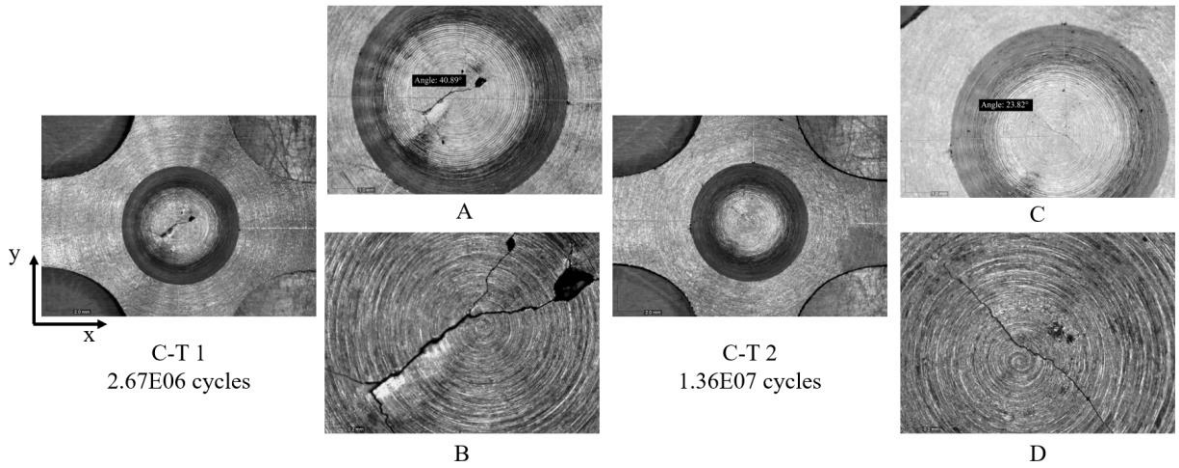

Fig. 12. C-T 1 (σ_y=144.3 MPa; σ_x=137 MPa; Cycles to failure = 2.67E6) and C-T 2 (σ_y=133.1 MPa; σ_x=124 MPa; Cycles to failure = 13.6E6): (A) and (C) crack initiation angle, respectively; (B) and (D) crack growth positioning, respectively.

The new N T-T specimens presented crack initiation at the arms' fillets which was not initially predicted. Thermal imaging proved the existence of heat generation at the midpoint and at the arms fillets, simultaneously. The fillet failure is associated with the presence of both resonant modes, MI and PM, within the frequency range. Both MI and PM have a high stress combination at the fillets in T-T specimens. The lower fillet combination stress to the midpoint in MI was increased by PM flapping motion, and thus failure occurred in the non-desired region. Damage at the corners, which could have been caused by poor machining, was observed. The surface damage may have contributed to stress concentration and crack initiation. Figure 13 shows the two present crack locations, size, the damaged surface, as well as thermal imaging where slight heat generation can be seen at the failed fillet.

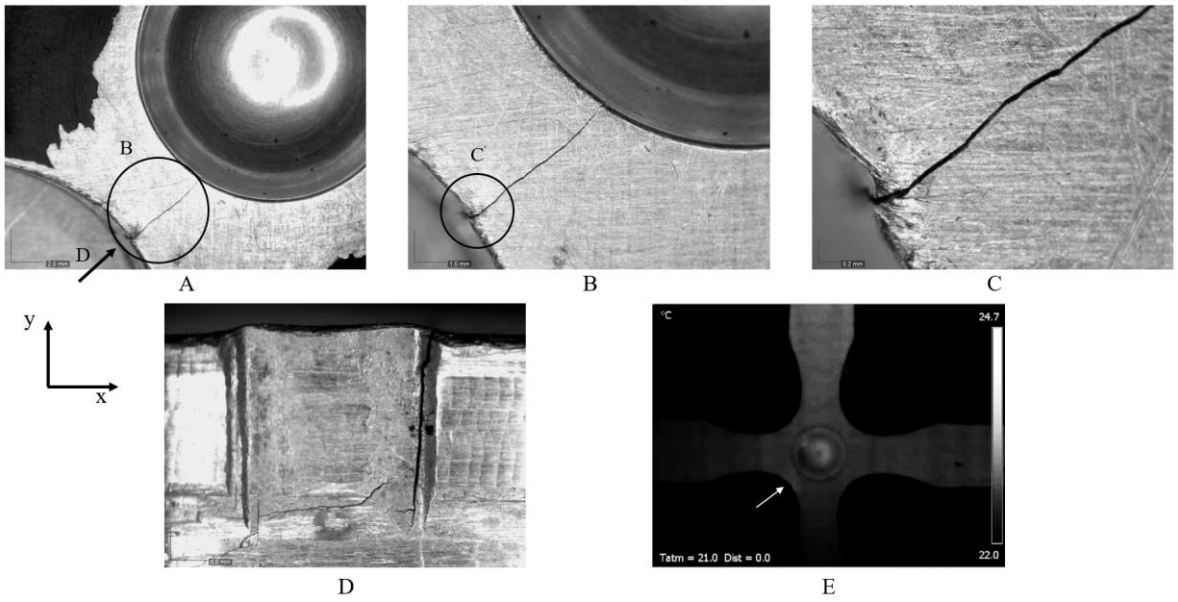

Fig. 13. N1 T-T (σ_y=112.5 MPa; σ_x=107.1 MPa; Cycles to failure = 12.1E6): (A) fatigue crack initiation; (B), (c) an (D) details of crack growth shape; (E) Thermal image of midpoint and fillet heat generation, indicated by the white arrow.

However, experimental analysis has shown that the PM effect at the midpoint is negligible in terms of induced stresses. These results highlight the importance of surface quality at the fillets and the need to further optimise the T-T geometry, ensuring a considerably higher stress combination at the midpoint. The F3 T-T specimen showed no visible heat generation at the fillets and a clear and single 53.9º crack initiation. F3 T-T presented a better and no damaged surface quality at the arms fillet. Figure 14 presents the crack path, initiation angle and location.

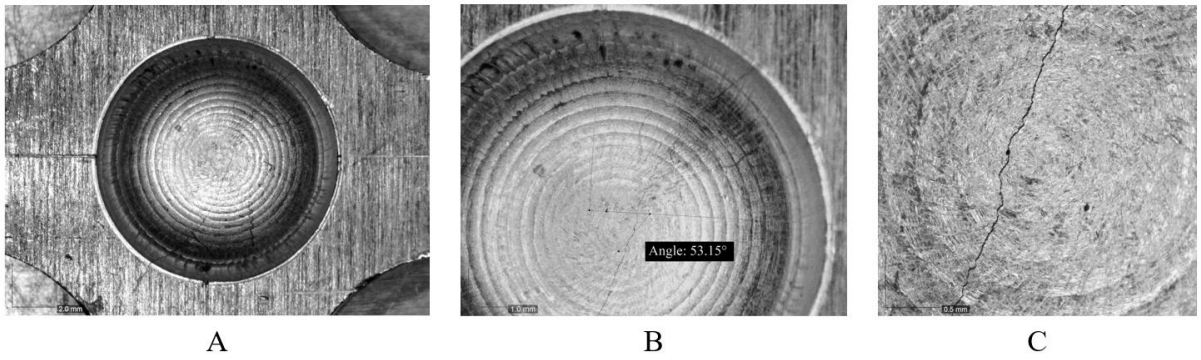

Fig. 14. F3 T-T (σ_y=176.48 MPa; σ_x=174.96 MPa; Cycles to failure = 0.76E6): (A) initial fatigue crack; (B) fatigue crack angle; (C) details of crack growth shape.

Initial crack growth under ultrasonic loading conditions displays similar patterns to conventional methods when correctly designed, and manufactured specimens are led to failure. Other authors have already described, both analytically and experimentally, the branching found in out-of-phase and one singular crack in in-phase specimens. Once the initial crack length becomes significant, further propagation in ultrasonic testing is no longer symmetric between the two growing crack tips. The branching found in 40-50º angle crack C-T is close to symmetrical as found by Garcia et al. [25] but with different angles between branches on each crack tip. After considerable crack propagation, the behaviour no longer presents full symmetry. The non-symmetrical, and in some specimens, chaotic behaviour is associated with the specimen resonance change with crack propagation. As the crack size increases, the specimen rigidity changes, thus changing its resonance frequency and mode shape. Numerical analyses with different initial cracks are required to characterise crack propagation and the occasional final chaotic behaviour.

5. Conclusions

In this work, a new method for ultrasonic fatigue testing of equibiaxial and pure shear cruciform specimens is presented and evaluated. Three different geometries of cruciform specimens were analysed and tested in an ultrasonic fatigue machine. An initial detailed modal analysis was conducted on a few specimens of each geometry. Two different laser-measured setups for the modal analysis were conducted based on finite element analysis. From the modal analysis, and as predicted by FEA, two modes with similar frequency can be excited by the ultrasonic setup: (i) An undesirable resonant mode, called the Parasite mode (PM); (ii) and the intended to be induced, the resonant Mode of Interest (MI).

Frequency Domain Decomposition (FDD), the followed modal analysis method, showed both MI and PM frequency for all analysed specimens. Even when one of the resonant modes was outside the working transducer frequency the FDD method allowed for its frequency determination. From FDD, the frequency variability of the tested specimens was possible to quantify, as well as the proximity of the PM mode and its negative impact on the final MI shape.

The first machined in-phase cruciform geometry (Fx T-T) presented high-frequency variability between specimens. Specimens presented one or both modes within the transducer working frequency. In future ultrasonic cruciform tests or other complex ultrasonic tests, the FDD method is recommended for variability quantification, PM frequency and influence determination. As the cruciform geometry is improved and later geometry standardisation, the FDD modal analysis method may no longer be required. Only one of the F T-T specimens (F3) proved to be fully working as intended. All other F T-T tested specimens showed a PM within the working frequency range with a non-negligible influence on the dynamic response of the MI. New in phase T-T and C-T specimens had similar displacement behaviours to the only working First T-T specimen. Thermal imaging reinforced the FE determined MI and PM behaviour.

Strain gauges were subsequently applied to experimentally prove that the specimens were working correctly. Having determined the axial-axial stress ratio and power to stress relation for all the tested cruciform specimens, fatigue analysis was conducted until failure. Following a laser or FDD analysis, strain gauges should be applied to all proven working cruciform specimens for fatigue testing. Future research will discard the need for strain gauges in all tested specimens. But just as uniaxial ultrasonic fatigue testing, one strain gauge will always be recommended to be applied in a first calibration specimen. All fatigue tested specimens showed lower lives for higher stress combinations. PM cruciform specimens presented multiple crack initiation in between arms fillets. All C-T and F3 T-T cruciform specimens presented fatigue crack initiations at the central circle. All such fractures are consistent with observations from other researchers, both from FEA and conventional fatigue testing. The new N T-T geometries showed unpredictable failure at the fillets. The cause was linked to both the presence of a PM and the in-phase axial-axial stress distribution, resulting in a high stress combination at the corners. The machining quality resulting in considerable surface damage at the fillets also showed to be determinant, creating the higher stress combinations outweighing the midpoint induced biaxial stress. Surface treatment in the arms fillets is therefore strongly recommended to ensure no stress concentration locations that can cause crack initiation.

Acknowledgements

This work was supported by FCT, through IDMEC, under LAETA, project UID/EMS/50022/2020. Financial support from Portuguese Fundação para a Ciência e Tecnologia (FCT) is acknowledged through project PTDC/EMS- PRO/5760/2014. The authors would also like to acknowledge Pedro Teixeira and João Vicente for assisting in specimen preparation.

References

[1] M. de Freitas, “Multiaxial fatigue: From materials testing to life prediction,” *Theor. Appl. Fract. Mech.*, **92**, 360–372, (2017).

[2] T., Naito, H. Ueda, M. Kikuchi, “Fatigue behavior of carburised steel with internal oxides and nonmartensitic micro-structure near the surface,” *Metall. Trans.*, **15 A**, 1431–1436, (1984).

[3] C. Bathias, “There is no infinite fatigue life in metallic materials,” *Fatigue Fract. Eng. Mater. Struct.*, **22**, 559–565, (1999).

[4] C. Bathias and P. C. Paris, *Gigacycle fatigue in mechanical practice*. 2005.

[5] I. Marines, X. Bin, and C. Bathias, “An understanding of very high cycle fatigue of metals,” *Int. J. Fatigue*, **25**, 9–11, 1101–1107, (2003).

[6] B. Zettl, H. Mayer, C. Ede, and S. Stanzl-Tschegg, “Very high cycle fatigue of normalized carbon steels,” *Int. J. Fatigue*, **28**, 11, 1583–1589, (2006).

[7] H. Q. Xue, H. Tao, F. Montembault, Q. Y. Wang, and C. Bathias, “Development of a three-point bending fatigue testing methodology at 20 kHz frequency,” *Int. J. Fatigue*, **29**, 2085–2093, (2007).

[8] R. Schuller, H. Mayer, A. Fayard, M. Hahn, and M. Bacher-Höchst, “Very high cycle fatigue of VDSiCr spring steel under torsional and axial loading,” *Materwiss. Werksttech.*, **44**, 4, 282–289, (2013).

[9] A. Nikitin, C. Bathias, and T. Palin-Luc, “A new piezoelectric fatigue testing machine in pure torsion for ultrasonic gigacycle fatigue tests: Application to forged and extruded titanium alloys,” *Fatigue Fract. Eng. Mater. Struct.*, **38**, 11, 1294–1304, (2015).

[10] P. Costa *et al.*, “Review of multiaxial testing for very high cycle fatigue: From ‘Conventional’ to ultrasonic machines,” *Machines*, **8**, 2, (2020).

[11] R. A. Cláudio, L. Reis, and M. Freitas, “Biaxial high-cycle fatigue life assessment of ductile aluminium cruciform specimens,” *Theor. Appl. Fract. Mech.*, **73**, 82–90, (2014).

[12] A. A. Shanyavskii, “Aluminium alloy under biaxial loading,” **19**, 12, (1996).

[13] A. Smits, D. Van Hemelrijck, T. P. Philippidis, and A. Cardon, “Design of a cruciform specimen for biaxial testing of fibre reinforced composite laminates,” *Compos. Sci. Technol.*, **66**, 7–8, 964–975, (2006).

[14] M. Quaresimin, L. Susmel, and R. Talreja, “Fatigue behaviour and life assessment of composite laminates under multiaxial loadings,” *Int. J. Fatigue*, **32**, 1, 2–16, (2010).

[15] C. Bathias, “Piezoelectric fatigue testing machines and devices,” *Int. J. Fatigue*, **28**, 11, 1438–1445, (2006).

[16] C. Brugger, T. Palin-Luc, P. Osmond, and M. Blanc, “Gigacycle fatigue behavior of a cast aluminum alloy under biaxial bending: experiments with a new piezoelectric fatigue testing device,” *Procedia Struct. Integr.*, **2**, 1179–1180, (2016).

[17] P. Costa, M. Vieira, L. Reis, A. Ribeiro, and M. de Freitas, “New specimen and horn design for combined tension and torsion ultrasonic fatigue testing in the very high cycle fatigue regime,” *Int. J. Fatigue*, **103**, 248–257, (2017).

[18] D. Montalvão and A. Wren, “Redesigning axial-axial (biaxial) cruciform specimens for very high cycle fatigue ultrasonic testing machines,” *Heliyon*, **3**, 11, e00466, (2017).

[19] D. Montalvão, A. Blaskovics, P. R. da Costa, L. Reis, and M. Freitas, “Numerical Analysis of VHCF Cruciform Test Specimens with Non-Unitary Biaxiality Ratios,” *Int. J. Comput. Methods Exp. Meas.*, **7**, 4, 327–339, (2019).

[20] P. R. da Costa, D. Montalvão, M. Freitas, R. Baxter, and L. Reis, “Cruciform specimens’ experimental analysis in ultrasonic fatigue testing,” *Fatigue Fract. Eng. Mater. Struct.*, **42**, 11, 2496–2508, (2019).

[21] R. Baptista, L. Reis, I. Guelho, M. Freitas, and J. F. A. Madeira, “Design optimization of cruciform specimens for biaxial fatigue loading,” *Frat. ed Integrita Struct.*, **30**, 118–126, (2014).

[22] R. Brincker and L. Zhang, “Frequency Domain Decomposition Revisited,” *Proc. 3rd Int. Oper. Modal Anal. Conf.*, (2009).

[23] Y. Lage, A. M. R. Ribeiro, D. Montalvão, L. Reis, and M. Freitas, “Automation in Strain and Temperature Control on VHCF with an Ultrasonic Testing Facility,” *Appl. Autom. Technol. Fatigue Fract. Test. Anal.*, 80–100, (2014).

[24] Y. Lage, H. Cachão, L. Reis, M. Fonte, M. De Freitas, and A. Ribeiro, “A damage parameter for HCF and VHCF based on hysteretic damping,” *Int. J. Fatigue*, **62**, 2–9, (2014).

[25] D. Infante-García, G. Qian, H. Miguélez, and E. Giner, “Analysis of the effect of out-of-phase biaxial fatigue loads on crack paths in cruciform specimens using XFEM,” *Int. J. Fatigue*, **123**, January, 87–95, (2019).

[26] E. U. Lee and R. E. Taylor, “Fatigue behavior of aluminum alloys under biaxial loading,” *Eng. Fract. Mech.*, **78**, 8, 1555–1564, (2011).

[27] C. H. Wolf, S. Henkel, A. Burgold, Y. Qiu, M. Kuna, and H. Biermann, “Investigation of fatigue crack growth under in-phase loading as well as phase-shifted loading using cruciform specimens,” *Int. J. Fatigue*, **124**, February, 595–617, (2019).

Declaration of interests

☒ The authors declare that they have no known competing financial interests or personal relationships that could have appeared to influence the work reported in this paper.

☐The authors declare the following financial interests/personal relationships which may be considered as potential competing interests:
